Journal of Analysis and Testing (2025) 9:575–583
https://doi.org/10.1007/s41664-025-00400-y

ORIGINAL PAPER

Multi-Level Engineering of Staggered Band Alignment Heterojunctions and Au@CeO_2 Yolk-Shell Nanozyme for Photoelectrochemical Biosensing Under Zero-Bias Conditions

Yu Du[1] · Rui Feng[1] · Tingting Wu[2] · Xue Dong[2] · Hongying Jia[2] · Dongquan Leng[2] · Huangxian Ju[2] · Qin Wei[2,3]

Received: 7 May 2025 / Accepted: 17 July 2025 / Published online: 13 November 2025

Abstract

The integration of artificial nanozymes with photoelectrochemical (PEC) biosensing remains underexplored, primarily due to challenges in balancing catalytic efficiency, material stability, and interfacial charge dynamics. Herein, we present a novel split-type PEC biosensor that leverages Au@CeO_2 yolk-shell nanozymes with robust phosphatase-mimicking activity and staggered band structure of WO_3/$BiVO_4$ heterojunction for ultrasensitive detection of the breast cancer biomarker HER-2. Unlike conventional nanoenzymes, the yolk-shell architecture encases Au NPs within a CeO_2 shell, synergistically enhancing catalytic efficiency by maximizing the active surface area while simultaneously preventing nanoparticle aggregation and leaching through a protective barrier. Density functional theory (DFT) calculations reveal that the CeO_2(111)/Au(111) interface drastically reduces the energy barrier for phosphate ester bond cleavage (-16.94 eV vs. 5.69 eV for free molecules), thereby enabling rapid hydrolysis of ascorbic acid 2-phosphate (AAP) into ascorbic acid. This catalytic amplification strategy, when integrated with a visible-light-responsive semiconductor substrate, enables zero-bias detection and while effectively eliminating interference from high-voltage operations. The biosensor achieves a detection limit of 41 fg/mL (*S/N*=3) for HER-2 across a linear range of 0.0001 −100 ng/mL, surpassing existing methods. Remarkable selectivity, reproducibility (RSD=3.9%), and recovery rates (95.1%–102.4%) in serum further validate its clinical applicability. This work establishes a universal platform for nanozyme-driven PEC biosensing, presenting significant promise for future use in pathological diagnostics.

Keywords Heterojunctions · Au@CeO_2 nanozymes · Biosensor · Photoelectrochemical detection · HER-2

1 Introduction

In recent years, the integration of electrochemical and optical methodologies has positioned photoelectrochemical (PEC) technology as a promising technique for biological analysis and detection [1–5]. The core principle of PEC involves the proton absorption-induced separation of photogenerated electrons and holes in the valence band of excited semiconductor nanomaterials [6–14]. By capitalizing on the properties of target substances or labeled materials to modulate electron transfer processes, quantitative detection can be achieved [15–18]. Although current PEC immunoassays primarily focus on the direct conjugation of nanomaterials with biological proteins [19–22], recent findings highlight a novel advantage in immunoassay design, spatially separating the biological molecular recognition module from the photoelectrochemical signal conversion unit [23, 24]. This

✉ Dongquan Leng
wlkqldq@163.com

✉ Huangxian Ju
hxju@nju.edu.cn

✉ Qin Wei
sdjndxwq@163.com

[1] School of Water Conservancy and Environment, University of Jinan, Jinan 250022, China

[2] Key Laboratory of Interfacial Reaction and Sensing Analysis in Universities of Shandong, School of Chemistry and Chemical Engineering, Collaborative Innovation Center for Green Chemical Manufacturing and Accurate Detection, University of Jinan, Jinan 250022, China

[3] Department of Chemistry, Sungkyunkwan University, Suwon 16419, Republic of Korea

strategy effectively minimizes interference from complex biomolecules with photoelectrochemical processes. This split-type PEC biosensing strategy boasts enhanced repeatability, high sensitivity, and reduced background signals.

Biological enzymes, protein-based catalysts produced by the cells of living organisms, are essential in bioanalysis due to their selective binding to target substances [25, 26]. Despite their excellent catalytic efficiency, the practical application of these enzymes is limited by high extraction and purification costs, as well as their vulnerability to inactivation under non-physiological conditions Artificial nanozymes, by contrast, offer broad utility, retaining enzyme-like catalytic abilities even in harsh environments [27–30]. Integrating highly efficient artificial nanozymes into advanced inorganic semiconductor materials thus opens new avenues for pathological analyses and physiological monitoring. CeO_2, acting as a Lewis acid, possesses phosphatase-like catalytic activity capable of facilitating the hydrolysis of phosphoric acid bonds [31–37]. While the inclusion of precious metals can enhance catalytic performance, this approach may also result in the aggregation and detachment of metal particles from the catalyst surface. By employing a core-shell design that encapsulates precious metals within CeO_2, we can shield the inner metal particles while maximizing the catalytic interface. In this study, we developed an Au@CeO_2 yolk-shell nanocomposite, where gold nanoparticles serve as the core and cerium dioxide forms the shell. This novel structure exhibits efficient phosphatase-like catalytic activity, effectively facilitating the hydrolysis of ascorbic acid 2-phosphate (AAP) to yield ascorbic acid.

HER-2, a transmembrane receptor bearing tyrosine kinase activity, critically affects tumor development in breast cancer and other malignancies [38, 39]. Its overexpression serves as a critical biomarker for assessing disease severity, guiding therapy, and selecting targeted drugs [40, 41]. The extracellular domain of HER-2 can be cleaved by proteases and released into the bloodstream [42], presenting a potential strategy for rapid serological detection via PEC devices. Meanwhile, WO_3 demonstrates favorable biocompatibility, stability and appropriate band gap for PEC [43, 44] but suffers from limited light absorption capability. To mitigate this issue, we adopt a type II heterojunction by depositing $BiVO_4$ onto WO_3 using successive ionic layer adsorption and reaction (SILAR) to enhance light energy absorption and electron-hole pair separation.

In this work, we have refined the preparation of a homogeneous electrolyte solution using our Au@CeO_2 yolk-shell nanozymes, which replaces the conventional phosphoenzyme-based controlled-release strategy. Density functional theory (DFT) calculations and experimental results substantiate the exceptional catalytic efficiency of the core-shell structure as a Lewis acid, proficiently facilitating the hydrolysis of phosphate bonds. Furthermore, we constructed a WO_3/$BiVO_4$ semiconductor heterojunction with enhanced light energy absorption efficiency, enabling zero-bias detection of trace electron donors. To illustrate the practical advantages, we selected HER-2 as a model analyte to establish a reliable platform for clinical diagnostics.

2 Experimental

2.1 Apparatus and Materials

Materials, apparatus and other experimental details were described in *Supporting Information*.

2.2 Preparation of WO_3/$BiVO_4$

The synthesis of WO_3/$BiVO_4$ heterostructures commenced with the preparation of a WO_3 film on F-doped tin oxide (FTO) glass. A solution was prepared by dissolving 0.231 g $Na_2WO_4{\cdot}2H_2O$ in 20 mL deionized water, followed by a slow addition of 20 mL 1.5 M hydrochloric acid, with continuous stirring. The mixture was combined with 30 mL solution containing 0.016 mol ammonium oxalate and stirring continued until the solution became clear. The resulting solution was transferred to a Teflon reactor and heated at 120 °C for 12 h, with the FTO glass placed conductively downward. After synthesis, the product was repeatedly washed with ultrapure water and ethanol, then vacuum-dried at 50 °C. For the WO_3/$BiVO_4$ synthesis, a successive ionic layer adsorption and reaction (SILAR) method was used [45]. Solution A was prepared by mixing 20 mL of acetic acid with ultrapure water (volume ratio of 1:19) and 5 mmol $Bi(NO_3)_3{\cdot}5H_2O$. Solution B was prepared by mixing 20 mL of ultrapure water with 5 mmol ammonium vanadate. The FTO/WO_3 electrode was sequentially immersed in solution A for 30 s, followed by solution B for an additional 30 s. This process was repeated for 10 cycles. The electrodes were air-dried and then calcined in a muffle furnace at 450 °C for 2 h. 1 cm^2 of the area covered by the material was reserved for future use.

2.3 Preparation of Au@CeO_2 yolk-shell Structure

The Au@CeO_2 yolk-shell structure was prepared by first combination of 1.6 mL of a solution containing 0.0466 g $Co(NO_3)_2{\cdot}6H_2O$ and 0.4 mL of a 2% $HAuCl_4$ solution in 50 mL ultrapure water. After refluxing the mixture at 70 °C, 3 mL of 2.5% ammonia solution was added and the reaction was heated for 10 min. Subsequently, 6 mL of a solution containing 0.087 g of $Ce(NO_3)_3{\cdot}6H_2O$ was added, and the mixture was stirred for 30 min. Following centrifugation

and ethanol washing, the products were re-dispersed in 50 mL of water with the addition of 15 µL hydrochloric acid, followed by stirring at 70 °C for 1 h. The final yolk-shell structured product was obtained after centrifugation and overnight drying at 50 °C (Fig. 1a).

2.4 Preparation and Testing Procedure of the Biosensor

The working electrode employed the prefabricated FTO/WO_3/$BiVO_4$ photoanode. A microplate served as the recognition platform. First, 50 µL Ab_1 was added to ensure strong antibody binding to the microplate, followed by overnight incubation. To prevent non-specific binding, the samples were treated with 1% bovine serum albumin (BSA) solution and incubated at 37 °C for 45 min to block active sites. After removing the excess BSA, the microplate was prepared for HER-2 antigen introduction. Different concentrations of HER-2 antigen were added to the microplate and incubated for 45 min at 37 °C. To complete the sandwich structure, 50 µL of the prepared Au@CeO_2-Ab_2 solution was added to the microplate. After each layer modification, the microplate was washed with PBS (pH 7.4). The final step involved adding 100 µL of a 50 mM ascorbic acid 2-phosphate solution, serving as the catalyzed substrate. The microplate containing this solution was incubated for a designated period to facilitate catalytic reaction. Upon completion, the resulting solution was carefully transferred to an electrolyte solution (0.1 M PBS) and subjected to photocurrent testing to assess biosensor performance (Fig. 1b). An LED lamp (100 W, 400–700 nm) was used as an irradiation source for PEC detection.

3 Results and Discussion

3.1 Characterization of WO_3/$BiVO_4$ and Au@CeO_2

The physical properties of WO_3/$BiVO_4$ photoanode materials and Au@CeO_2 secondary antibody markers were evaluated using Transmission Electron Microscopy (TEM), Scanning Electron Microscopy (SEM), and X-ray Diffraction (XRD). XRD analysis (Fig. 2a) revealed distinct diffraction peaks for WO_3 at 23.14°, 23.64°, 24.34°, 28.4°, 28.87°, 33.58°, 33.93°, 34.47°, and 47.253°, corresponding to the (002), (020), (200), (-112), (112), (-202), (-220), (220), and (004) crystal planes, respectively, in accordance with standard JCPDS card No. 20-1323. Additionally, the peaks observed for the nanocomposites align with the (110) and (-121) crystal planes of the JCPDS card No. 14–0688 at 18.67° and 28.822°, respectively. SEM images in Fig. 2b display the uniform sheet-like structure of WO_3 on the FTO surface, while Fig. 2c presents the coral-like morphology of $BiVO_4$. Figure 2d reveals the growth of $BiVO_4$ nanoparticles on the WO_3 surface, forming a well-integrated heterojunction structure. The TEM and high-resolution TEM (HTEM) images of Au@CeO_2 (Fig. 2e-g) depict the core-shell structure, with Au serving as the core and CeO_2 forming the shell. The nanoparticles are uniformly dispersed, with sizes ranging from 70 to 100 nm. A lattice spacing of 0.235 nm, observed in Fig. 2g, corresponds to the (111) crystal plane of Au, confirming the successful preparation of the Au@CeO_2 nanostructures. Energy Dispersive Spectroscopy (EDS) analysis and mapping (Fig. 2h-l) further validate the presence of Bi, O, V, and W elements in the

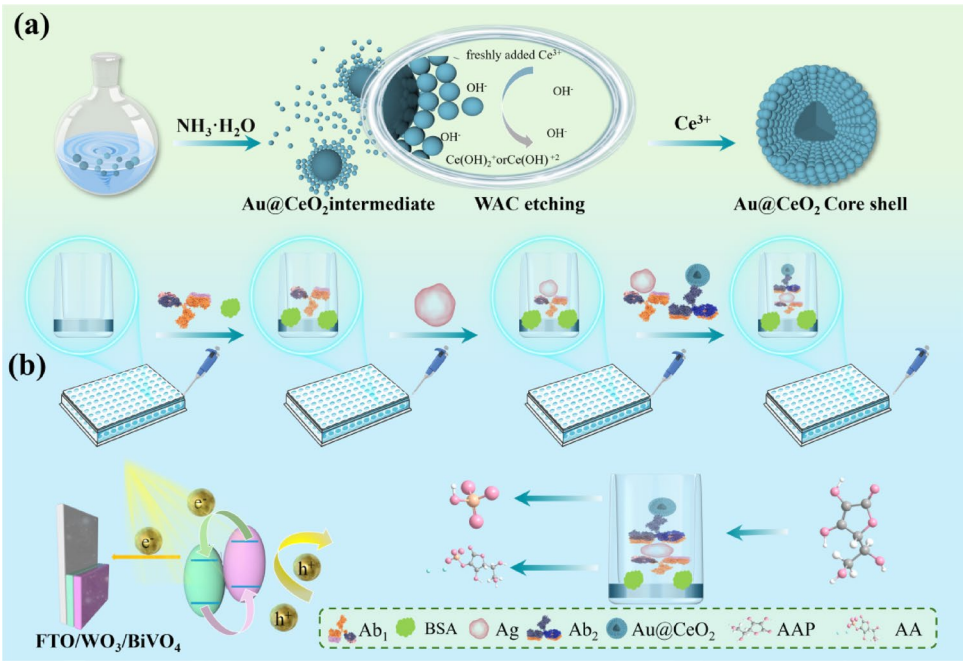

Fig. 1 Fabrication process of PEC biosensor. **a** Preparation of Au@CeO_2. **b** Preparation and testing procedure of the biosensor

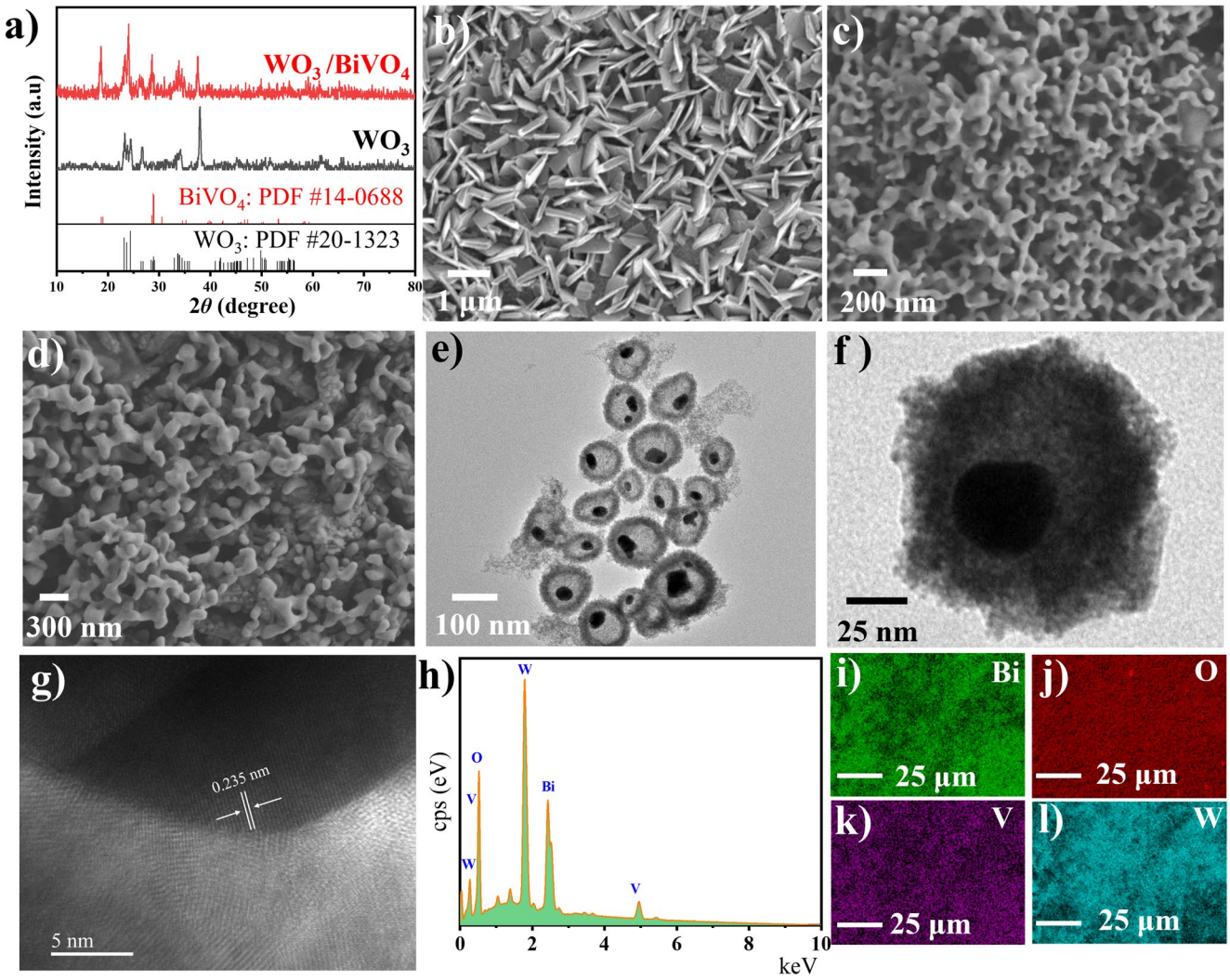

Fig. 2 **a** XRD patterns of WO_3 and $WO_3/BiVO_4$. SEM images of **b**WO_3, **c** $BiVO_4$ and **d** $WO_3/BiVO_4$. **e**, **f** TEM images of Au@CeO_2. **g** HRTEM image of Au@CeO_2. **h** EDS spectrum and **i-l** mapping of $WO_3/BiVO_4$

composite, providing additional evidence for the successful synthesis of the intended structures.

To further investigate the chemical composition and the corresponding element valence state of the $WO_3/BiVO_4$ composite, X-ray photoelectron spectroscopy (XPS) was employed. As shown in Fig. 3 and Fig. S1, the XPS spectra reveal characteristic peaks for the elements of W, Bi, V, O present in the composite. The W 4f spectrum displays two prominent peaks, W $4f_{5/2}$ and W $4f_{7/2}$, located at 36.98 eV and 34.88 eV, respectively (Fig. 3a). The Bi 4f peaks, corresponding to Bi^{3+}, are observed at 158.68 eV and 163.98 eV, matching well with the Bi $4f_{7/2}$ and Bi $4f_{5/2}$ orbitals (Fig. 3b). The V $2p_{1/2}$ and V $2p_{3/2}$ peaks at 523.8 eV and 516.3 eV, respectively, align with the previously reported [46] peak positions of V^{5+} in $BiVO_4$ (Fig. 3c). The two predominant oxygen peaks at 529.48 eV and 531.08 eV are attributed to lattice oxygen, while the peak at 532.48 eV corresponds to adsorbed H_2O or surface hydroxyl group (-OH) (Fig. 3d).

3.2 Experimental Optimization, Electrochemical Characterization, and DFT Calculations

The catalytic efficiency of artificial nanozymes per unit of time and the composition of the electrolyte solution are critical factors affecting the performance of the biosensor. Initially, the catalytic duration for Au@CeO_2 to cleave the phosphate ester bond was optimized, with photocurrent responses monitored at five-minute intervals. The data in Fig. 4a shows a sharp increase in the photocurrent during the first 25 min, followed by a subsequent reduction in the rate of change. Balancing sensor sensitivity and practical detection time, a 25-minute catalytic period was deemed optimal. Subsequent optimization focused on adjusting the pH of the

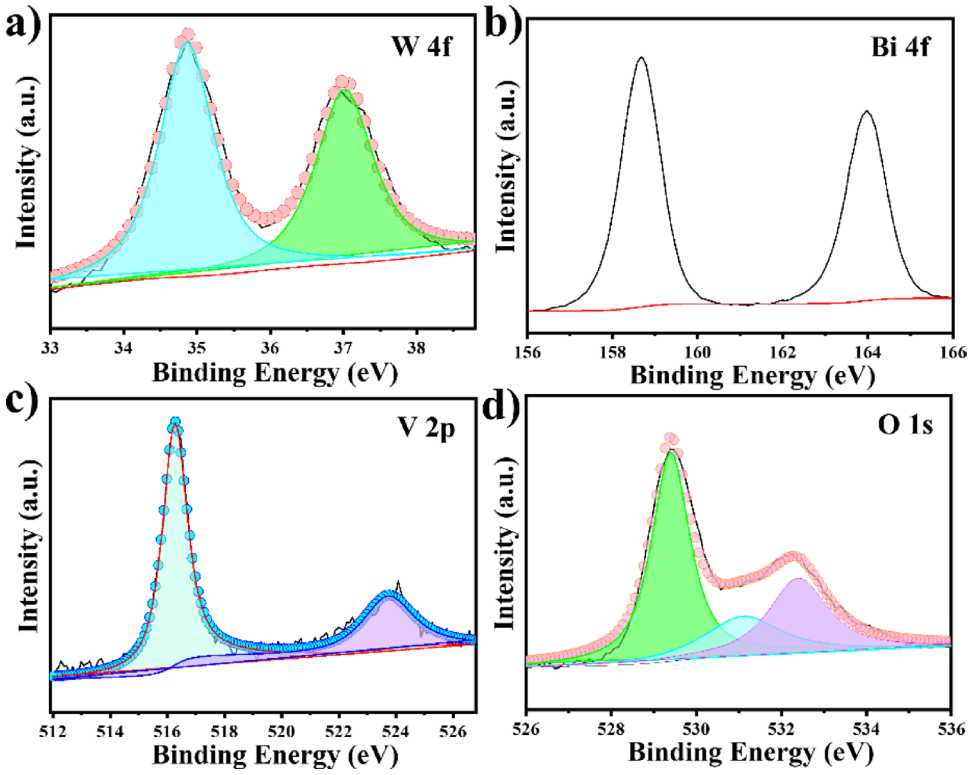

Fig. 3 XPS spectra of **a** W 4f, **b** Bi 4f, **c** V 2p, and **d** O 1s for WO_3/$BiVO_4$

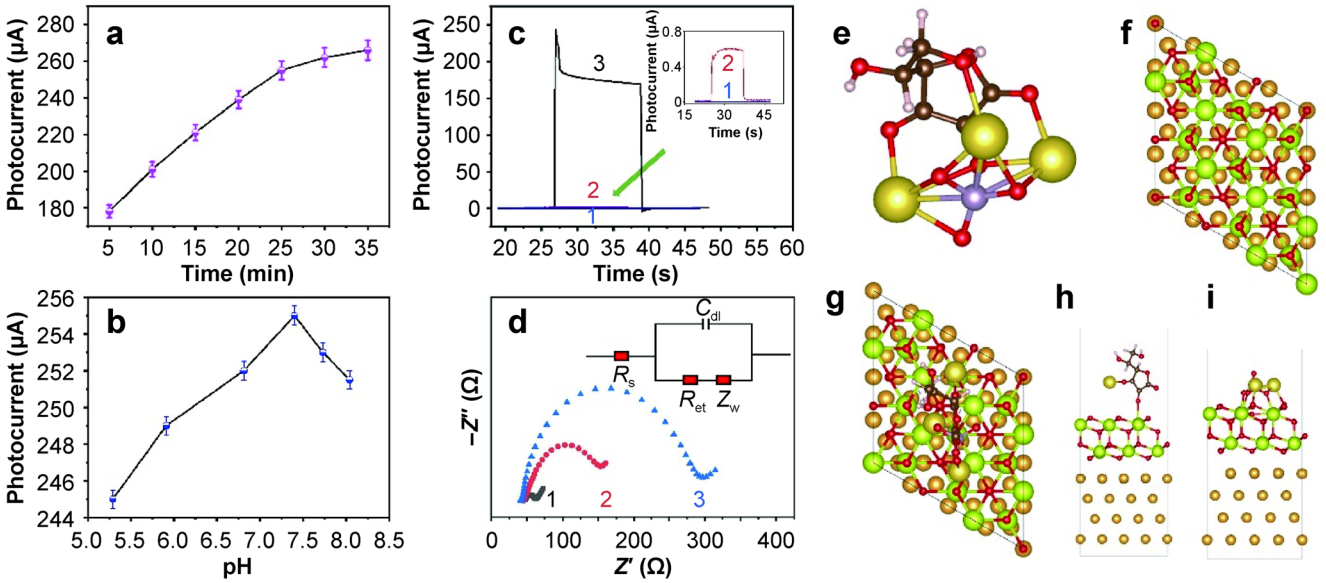

Fig. 4 **a** Catalytic time of Au@CeO_2 in 0.1 M PBS (pH 7.4) at 0 V (c_{HER-2} = 0.5 ng/mL), **b** Effect of pH of PBS on the photocurrent response of the photoanode in 0.1 M PBS (c_{HER-2} = 0.5 ng/mL). **c** PEC signal in 0.1 M PBS (pH 7.4) at 0 V, and **d** EIS in 0.1 M KCl containing 5.0 mM $[Fe(CN)6]^{3-/4-}$ of (1) ITO, (2) WO_3, and (3) ITO/WO_3/$BiVO_4$. **e** Molecular model of ascorbate phosphate salt, **f** Surface model of CeO_2(111)/Au(111) heterojunction, **g** Surface adsorption of the molecule, **h** Part 1 of phosphate ester bond breaking model, and **i** Part 2 of phosphate ester bond breaking model

electrolyte solution, with peak performance observed at pH 7.4 (Fig. 4b). The electrochemical properties of the photoelectric chemobiological sensor are crucial for confirming its successful fabrication. The photocurrent response of the photoanode modified with photoelectric materials was evaluated. As shown in Fig. 4c, the bare indium-tin-oxide (ITO) electrode exhibited no photocurrent, while the WO_3-coated electrode produced a faint response. Conversely, the presence of $BiVO_4$ significantly enhanced the photocurrent. This could be attributed to the low light absorption

efficiency of WO_3 alone and the enhanced electron-hole pair recombination efficiency resulting from the formation of the heterojunction structure. Moreover, electrochemical impedance spectroscopy (EIS), shown in Fig. 4d, revealed an increase in charge-transfer resistance (R_{ct}) with each modification layer, further supporting the successful construction of the sensor's working electrode.

To explore the phosphatase-like cleavage capability of the nanozyme, DFT was employed to analyze the CeO_2(111)/Au(111) heterojunction surface model's ability to cleave single ester bonds in AAP. The optimized structures of ascorbate phosphate and the heterojunction surface model are depicted in Fig. 4e and f, respectively. Additionally, the molecule's adsorption structure on the CeO_2(111)/Au(111) heterojunction surface is shown in Fig. 4g, while Fig. 4h and i illustrate the two resulting parts after phosphate ester bond cleavage. The dissociation energy of a single organic molecule was calculated to be 5.69 eV, while for the organic molecule adsorbed on the CeO_2(111)/Au(111) heterojunction surface, the energy was −16.94 eV, confirming the Au@CeO_2 yolk-shell nanozymes' capability to cleave phosphate ester bonds effectively.

3.3 Possible Mechanisms of PEC Detection

The PEC detection mechanism of the proposed biosensor relies on the synergistic interaction between the WO_3/$BiVO_4$ heterojunction and the Au@CeO_2 yolk-shell nanozyme. To further elucidate this mechanism, ultraviolet-visible diffuse reflectance spectroscopy (DRS) and Mott-Schottky (MS) analyses were conducted to explore the band structure and charge transfer behavior of the semiconductor materials. As shown in Fig. 5a, the DRS spectra of WO_3, $BiVO_4$, and WO_3/$BiVO_4$ heterojunction revealed distinct light absorption profiles. Pure WO_3 exhibited a narrow absorption edge at ~483 nm, corresponding to a 2.86 eV bandgap (calculated via the Tauc plot in Fig. 5b). In contrast, $BiVO_4$ demonstrated broader absorption, extending to ~536 nm, with a 2.23 eV bandgap (Fig. 5c). The WO_3/$BiVO_4$ heterojunction exhibited enhanced light absorption across the visible spectrum, attributed to the complementary bandgaps of the two materials. This extended absorption range facilitates efficient utilization of visible light for electron-hole pair generation. MS analysis was performed to determine the flat-band potentials (E_f) and semiconductor types of WO_3 and $BiVO_4$ (Fig. 5d, e). The positive slopes of the MS plots confirmed both materials as n-type semiconductors. The E_f values were calculated as 0.34 V vs. SCE for WO_3 and −0.13 V vs. SCE for $BiVO_4$. Based on the relationship $E_{CB} \approx E_f - 0.1$ V (for n-type semiconductors), the conduction band (CB) positions of WO_3 and $BiVO_4$ were estimated at 0.24 eV and −0.23 eV, respectively. The valence band (VB) positions, derived from $E_{VB} = E_{CB} + E_g$, were 3.1 eV (WO_3) and 2.0 eV ($BiVO_4$). The staggered band alignment between WO_3 and $BiVO_4$ forms a type II heterojunction, where photogenerated electrons in CB of $BiVO_4$ migrate to CB of WO_3, while holes in VB of WO_3 transfer to VB of $BiVO_4$. This spatial separation significantly suppresses

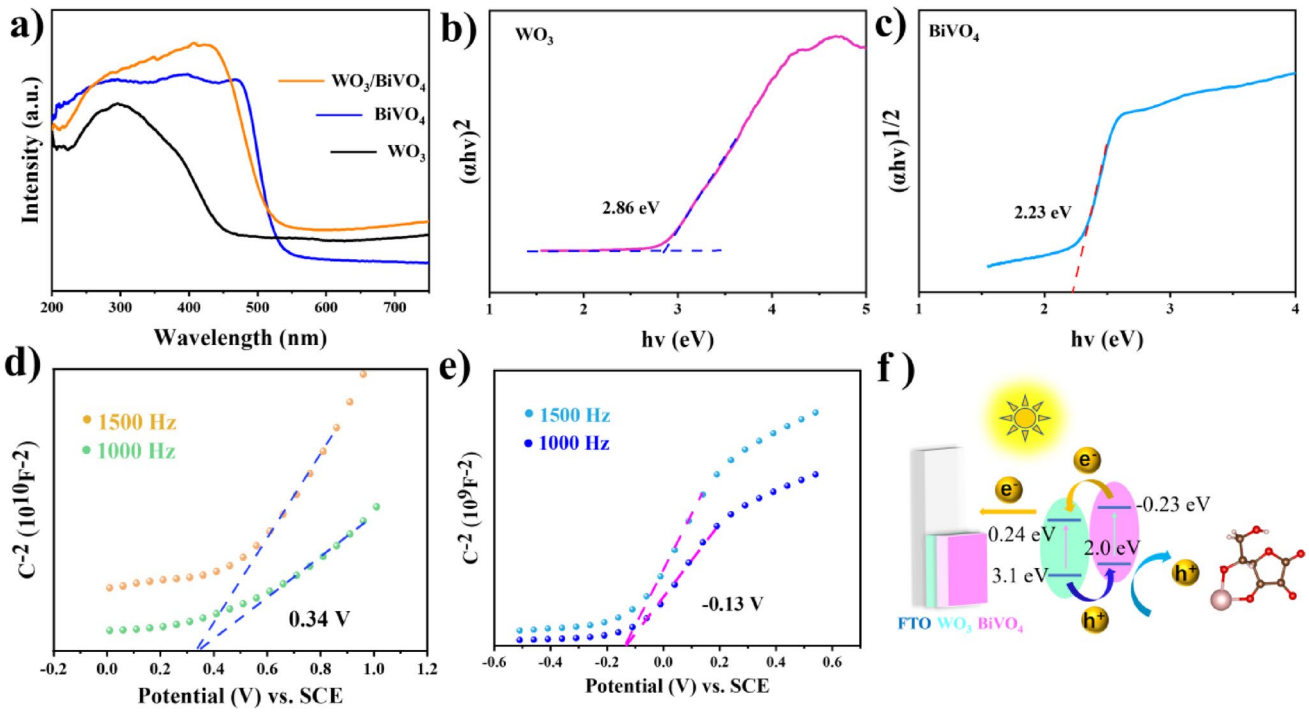

Fig. 5 **a** DRS images of WO_3, $BiVO_4$, and WO_3/$BiVO_4$. Tauc plots of **b** WO_3 and **c** $BiVO_4$. MS of **d** WO_3 and **e** $BiVO_4$. **f** Mechanism of PEC signal

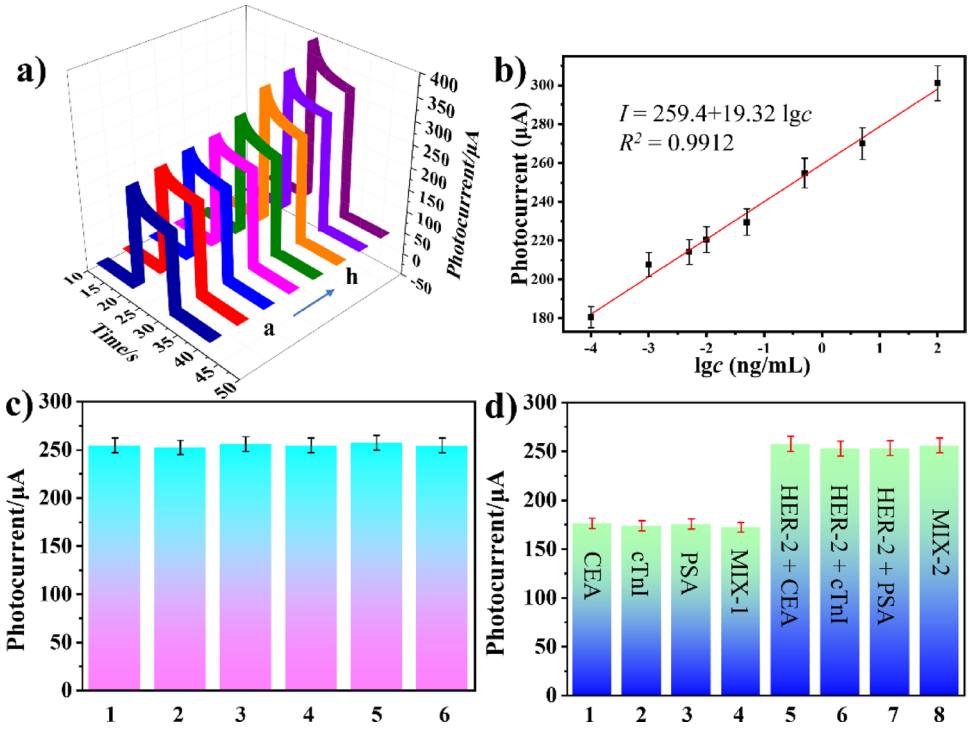

Fig. 6 **a** PEC signal in 0.1 M PBS (pH 7.4) containing the catalyzed solution at 0 V. **b** Standard curve for immunosensing of HER-2. **c** Reproducibility test in 0.1 M PBS (pH 7.4) at 0 V (c_{HER-2} = 0.5 ng/mL). **d** Selectivity test in 0.1 M PBS (pH 7.4) at 0 V (c_{HER-2} = 0.5 ng/mL)

electron-hole recombination and enhances photocurrent generation. The Au@CeO_2 yolk-shell nanozyme plays a dual role in the PEC detection process: the CeO_2 shell acts as a Lewis acid, catalyzing the hydrolysis of ascorbic acid 2-phosphate to ascorbic acid (AA), a strong electron donor, scavenges photogenerated holes at the WO_3/$BiVO_4$ surface, further accelerating charge separation and amplifying the photocurrent signal in Fig. 5f.

3.4 HER-2 Analysis

HER-2, a critical biomarker for therapeutic monitoring and prognosis in clinical settings, was chosen as the target analyte to evaluate the performance of the proposed biosensor. To this end, varying concentrations of HER-2 were placed in 96-well microtiter plates to produce solutions with distinct concentrations. These solutions were then transferred to an electrolyte solution to adjust the working curves accordingly. Under optimized experimental parameters, standard HER-2 samples at concentrations from 0.0001 to 100 ng/mL were examined to assess the biosensor's analytical capabilities, as shown in Fig. 6a (concentration points (a–h): 0.0001, 0.001, 0.005, 0.01, 0.05, 0.5, 5, and 100 ng/mL). A calibration curve was derived from the relationship between the logarithm of the antigen concentration and the photocurrent response, yielding the equation I=259.4+19.32 lg$c$ with R^2 of 0.9912, as displayed in Fig. 6b. The limit of detection for the biosensor was determined to be 41 fg/mL, based on a signal-to-noise ratio (S/N) of 3.

3.5 Performance of Biosensor

For biosensors deployed in clinical diagnostics, attributes such as stability, selectivity, and repeatability are paramount. The repeatability of the sensor was assessed by conducting 6 consecutive tests under uniform conditions, yielding a relative standard deviation (RSD) of 3.9%, as depicted in Fig. 6c. In evaluating selectivity, the presence of potential interferents such as cTnI, CEA and PSA were investigated. As shown in Fig. 6d, the photocurrent response in the presence of these individual interferents was similar to that of an unmodified electrode. Notably, when HER-2, the target analyte, was introduced, the sensor's response matched that of the reference substances, regardless of whether the test solution contained one or more interfering antigens. This confirms the biosensor's selectivity. Additionally, the sensor's stability was examined at a HER-2 concentration of 0.05 ng/mL, resulting in an RSD of 4.2%, as shown in Fig. S3.

3.6 Analysis of Serum Samples

To address potential compositional variations between serum and the prepared standard samples, the standard addition method was applied. After spiking the ten-fold diluted serum with varying concentrations of standard samples, the recovery rates, as shown in Table S2, ranged from 95.1% to 102.4%. Additionally, the RSDs for these measurements

ranged from 3.2% to 4.1%, highlighting the sensor's promising potential for clinical applications.

4 Conclusions

In summary, we have successfully developed a highly sensitive photoelectrochemical biosensor utilizing Au@CeO_2 yolk-shell nanozymes with phosphatase-like activity and a WO_3/$BiVO_4$ heterojunction photoanode. The innovative yolk-shell structure not only enhanced the catalytic efficiency of the nanozymes but also prevented the aggregation of precious metal particles, ensuring a stable and optimized catalytic interface. The density functional theory calculations provided insights into the catalytic mechanism, revealing that the CeO_2(111)/Au(111) interface significantly reduced the energy barrier for phosphate ester bond cleavage, thereby enhancing the catalytic activity of the nanozymes. By replacing conventional phosphoenzymes with Au@CeO_2 nanozymes, we achieved a controlled-release strategy that significantly improved the performance of the biosensor. The biosensor demonstrated excellent selectivity, reproducibility, and stability, making it a promising tool for clinical diagnostics.

Supporting Information Materials and reagents, Apparatus, preparation of Au@CeO_2-Ab_2, DFT calculations, XPS survey spectrum, side view of heterojunction surface model, stability test of biosensors and comparison with other methods were in Supporting Information.

Supplementary Information The online version contains supplementary material available at https://doi.org/10.1007/s41664-025-00400-y.

Acknowledgements This study was supported by the National Natural Science Foundation of China (No. 22206056, 22274062, 22574062, 22574063), the Shandong Provincial Natural Science Foundation (No. ZR2022QB117), Special Foundation for Taishan Scholar Professorship of Shandong Province. The authors would like to thank Scientific Compass (www.shiyanjia.com) for the support of XPS analysis.

Declarations

Conflict of interest The authors declare no competing financial interest.

References

1. Ban R, Li CJ, Xu YT, Zhu YY, Ju P, Li YM, Du HJ, Hu J, Chen G, Lin P, Zhao WW. Alkaline phosphatase-mediated bioetching of CoOOH/$BiVO_4$ for signal-on organic photoelectrochemical transistor bioanalysis. Anal Chem. 2023;95(2):1454–60.
2. Farka Z, Jurik T, Kovar D, Trnkova L, Skladal P. Nanoparticle-based immunochemical biosensors and assays: recent advances and challenges. Chem Rev. 2017;117(15):9973–10042.
3. Hu J, Lu MJ, Chen FZ, Jia HM, Zhou H, Li K, Zeng X, Zhao WW, Lin P. Multifunctional hydrogel hybrid-gated organic photoelectrochemical transistor for biosensing. Adv Funct Mater. 2022;32(26):2109046.
4. Tan R, Qin Y, Liu M, Wang H, Li J, Luo Z, Hu L, Gu W, Zhu C. Nickel single-atom catalyst-mediated efficient redox cycle enables self-checking photoelectrochemical biosensing with dual photocurrent readouts. ACS Sens. 2023;8(1):263–9.
5. Yang H, Zhou Q, Fang Z, Li W, Zheng Y, Ma J, Wang Z, Zhao L, Liu S, Shen Y, Zhang Y. Carbon nitride of five-membered rings with low optical bandgap for photoelectrochemical biosensing. Chem. 2021;7(10):2708–21.
6. Jiaju S, Zichao C, Chunqin Z, Meiqi S, Han L, Shusheng Z, Zhen Z. Photoelectrochemical biosensing platforms for tumor marker detection. Coord Chem Rev. 2022;469:214675.
7. Ye X, Wang X, Kong Y, Dai M, Han D, Liu Z. FRET modulated signaling: A versatile strategy to construct photoelectrochemical microsensors for in vivo analysis. Angew Chem Int Ed Engl. 2021;60(21):11774–8.
8. You F, Wei J, Cheng Y, Wen Z, Ding C, Hao N, Wang K. Selective and sensitive photoelectrochemical aptasensor for streptomycin detection based on Bi_4VO_8Br/Ti_3C_2 nanohybrids. J Hazard Mater. 2021;414:125539.
9. Leng D, Zhao J, Ren X, Xu R, Liu L, Liu X, Li Y, Wei Q. $MoSe_2$/CdSe heterojunction destruction by cation exchange for photoelectrochemical immunoassays with a controlled-release strategy. Anal Chem. 2021;93(30):10712–8.
10. Tang X, Lu C, Xu X, Ding Z, Li H, Zhang H, Wang Y, Li C. A visible and near-infrared light dual responsive signal-off and signal-on photoelectrochemical aptasensor for prostate-specific antigen. Biosens Bioelectron. 2022;202:113905.
11. Wang Z, Ning X, Feng Y, Zhang R, He Y, Zhao H, Chen J, Du P, Lu X. Insights into the enhanced photoelectrochemical performance through construction of the Z-Scheme and type II heterojunctions. Anal Chem. 2022;94(23):8539–46.
12. Xu R, Xu K, Du Y, Li J, Ren X, Ma H, Wu D, Li Y, Wei Q. Dual direct Z-scheme heterojunction with growing photoactive property for sensitive photoelectrochemical and colorimetric bioanalysis. Anal Chem. 2022;94(27):9888–93.
13. Yu Z, Gong H, Li Y, Xu J, Zhang J, Zeng Y, Liu X, Tang D. Chemiluminescence-derived self-powered photoelectrochemical immunoassay for detecting a low-abundance disease-related protein. Anal Chem. 2021;93(39):13389–97.
14. Wang CS, Zhou BY, Wang YF, Yuan C, Kou BH, Zhao WW, Xu JJ. Bifunctional iron-porphyrin metal-organic frameworks for organic photoelectrochemical transistor gating and biosensing. Chin Chem Lett. 2025;36(3):110080.
15. Yu SY, Zhang L, Zhu LB, Gao Y, Fan GC, Han DM, Chen G, Zhao WW. Bismuth-containing semiconductors for photoelectrochemical sensing and biosensing. Coord Chem Rev. 2019;393:9–20.
16. Zheng H, Zhang S, Yuan J, Qin T, Li T, Sun Y, Liu X, Wong DKY. Amplified detection signal at a photoelectrochemical aptasensor with a poly(diphenylbutadiene)-BiOBr heterojunction and Au-modified CeO_2 octahedrons. Biosens Bioelectron. 2022;197:113742.
17. Xu YT, Yuan C, Zhou BY, Li Z, Hu J, Lin P, Zhao WW, Chen HY, Xu JJ. Silicon solar cell-enabled organic photoelectrochemical transistor optoelectronics. Sci China Mater. 2023;66(5):1861–9.
18. Yu SY, Liu YL, Li Z, Jiang D, Xu JJ, Chen HY, Zhao WW. Nature-inspired design of droplet-synthesized polymeric nanoelectrode for photoelectrochemical MicroRNA sensing within single cells. Sci Bull. 2024;69(2):159–62.

19. Khan SU, Trashin S, Beltran V, Korostei YS, Pelmus M, Gorun SM, Dubinina TV, Verbruggen SW, De Wael K. Photoelectrochemical behavior of phthalocyanine-sensitized TiO_2 in the presence of electron-shuttling mediators. Anal Chem. 2022;94(37):12723–31.
20. Leng D, Li J, Xu R, Liu L, Liu X, Fan D, Wang H, Wei Q, Ju H. THCH as electron donor in controlled-release system for procalcitonin analysis based on $Bi_2Sn_2O_7$ photoanode. Sens Actuat B: Chem. 2020;321:128509.
21. Niu X, Lu C, Su D, Wang F, Tan W, Qu F. Construction of a polarity-switchable photoelectrochemical biosensor for ultrasensitive detection of miRNA-141. Anal Chem. 2021;93(40):13727–33.
22. Qin Y, Wen J, Zheng L, Yan H, Jiao L, Wang X, Cai X, Wu Y, Chen G, Chen L, Hu L, Gu W, Zhu C. Single-atom-based heterojunction coupling with ion-exchange reaction for sensitive photoelectrochemical immunoassay. Nano Lett. 2021;21(4):1879–87.
23. Zheng Y, Zhou Y, Cui X, Yan H, Cao L, Gao L, Yin H. Investigation of the effect of antibiotics on 5-formylcytosine content in Mazie seedling tissues based on photoelectrochemical biosensor. J Hazard Mater. 2022;436:129146.
24. Zhou Q, Tang D. Recent advances in photoelectrochemical biosensors for analysis of Mycotoxins in food. TrAC Trends Anal Chem. 2020;124:115814.
25. Ban R, Lu MJ, Hu J, Li CJ, Li YM, Gao G, Wang CS, Kong FY, Zhou H, Lin P, Zhao WW. Biological modulating organic photoelectrochemical transistor through in situ enzymatic engineering of photoactive gate for sensitive detection of serum alkaline phosphatase. Biosens Bioelectron. 2022;218:114752.
26. Cheng H, Lin S, Muhammad F, Lin YW, Wei H. Rationally modulate the oxidase-like activity of nanoceria for self-regulated bioassays. ACS Sens. 2016;1(11):1336–43.
27. Li X, Zhu H, Liu P, Wang M, Pan J, Qiu F, Ni L, Niu X. Realizing selective detection with nanozymes: strategies and trends. TrAC Trends Anal Chem. 2021;143:116379.
28. Qin Y, Wen J, Wang X, Jiao L, Wei X, Wang H, Li J, Liu M, Zheng L, Hu L, Gu W, Zhu C. Iron single-atom catalysts boost photoelectrochemical detection by integrating interfacial oxygen reduction and enzyme-mimicking activity. ACS Nano. 2022;16(2):2997–3007.
29. Zhao WW, Xu JJ, Chen HY. Photoelectrochemical enzymatic biosensors. Biosens Bioelectron. 2017;92:294–304.
30. Xu KX, Yuan C, Lou H, Chen FZ, Zhang L, Chen G, Han DM, Zhao WW. Metal-organic framework nanozyme enabling dual-functional photo-induced charge transfer and biomimetic precipitation for advanced organic photoelectrochemical transistor bioanalysis. Chin J Chem. 2024;42(17):1999–2004.
31. Gao M, Liu X, Wang Z, Wang H, Asset T, Wu D, Jiang J, Xie Q, Xu S, Cai X, Li J, Wang W, Zheng H, Gao X, Tarasenko N, Rotonnelli B, Gallet JJ, Jaouen F, Li R. Engineering catalytic dephosphorylation reaction for endotoxin inactivation. Nano Today. 2022;44:101456.
32. Liao X, Wang X, Li P, Chen S, Zhang M, Mei L, Qi Y, Hong C. Electrochemical immunosensor using artificial enzyme-induced metallization for the ultra-sensitive detection of alpha Fetoprotein. Sens Actuat B: Chem. 2021;344:130258.
33. Manto MJ, Xie P, Wang C. Catalytic dephosphorylation using ceria nanocrystals. ACS Catal. 2017;7(3):1931–8.
34. Tan Z, Wu TS, Soo YL, Peng YK. Unravelling the true active site for CeO_2-catalyzed dephosphorylation. Appl Catal B: Environ. 2020;264:118508.
35. Wang Q, Yi X, Chen YC, Xiao Y, Zheng A, Chen JL, Peng YK. Electronic-state manipulation of surface titanium activates dephosphorylation over TiO_2 near room temperature. Angew Chem Int Ed Engl. 2021;60(29):16149–55.
36. Yao T, Tian Z, Zhang Y, Qu Y. Phosphatase-like activity of porous nanorods of CeO_2 for the highly stabilized dephosphorylation under interferences. ACS Appl Mater Interfaces. 2019;11(1):195–201.
37. Zhao C, Xu Y. Theoretical investigation of dephosphorylation of phosphate monoesters on CeO_2(111). Catal Today. 2018;312:141–8.
38. Hanker AB, Brown BP, Meiler J, Marin A, Jayanthan HS, Ye D, Lin CC, Akamatsu H, Lee KM, Chatterjee S, Sudhan DR, Servetto A, Brewer MR, Koch JP, Sheehan JH, He J, Lalani AS, Arteaga CL. Co-occurring gain-of-function mutations in HER2 and HER3 modulate HER2/HER3 activation, oncogenesis, and HER2 inhibitor sensitivity. Cancer Cell. 2021;39(8):1099–114.e8.
39. Li BT, Ross DS, Aisner DL, Chaft JE, Hsu M, Kako SL, Kris MG, Varella-Garcia M, Arcila ME. HER2 amplification and HER2 mutation are distinct molecular targets in lung cancers. J Thorac Oncol. 2016;11(3):414–9.
40. Ni J, Kabraji S, Xie S, Wang Y, Pan P, He X, Liu Z, Leone JP, Long HW, Brown MA, Winer EP, Dillon DAR, Lin NU, Zhao JJ. p16(INK4A)-deficiency predicts response to combined HER2 and CDK4/6 Inhibition in HER2+breast cancer brain metastases. Nat Commun. 2022;13(1):1473.
41. Qaiser T, Mukherjee A, Reddy Pb C, Munugoti SD, Tallam V, Pitkaaho T, Lehtimaki T, Naughton T, Berseth M, Pedraza A, Mukundan R, Smith M, Bhalerao A, Rodner E, Simon M, Denzler J, Huang CH, Bueno G, Snead D, Ellis IO, Ilyas M, Rajpoot N. HER2 challenge contest: a detailed assessment of automated HER2 scoring algorithms in whole slide images of breast cancer tissues. Histopathology. 2018;72(2):227–38.
42. Wang T, Xu Y, Sheng S, Yuan H, Ouyang T, Li J, Wang T, Fan Z, Fan T, Lin B, Xie Y. HER2 somatic mutations are associated with poor survival in HER2-negative breast cancers. Cancer Sci. 2017;108(4):671–7.
43. Li Y, Mei Q, Liu Z, Hu X, Zhou Z, Huang J, Bai B, Liu H, Ding F, Wang Q. Fluorine-doped iron oxyhydroxide cocatalyst: promotion on the WO_3 photoanode conducted photoelectrochemical water splitting. Appl Catal B: Environ. 2022;304:120995.
44. Velmurugan S, Ching Juan TCKY, Chen J. Preparation of novel nanostructured WO_3/$CuMnO_2$ p-n heterojunction nanocomposite for photoelectrochemical detection of Nitrofurazone. J Colloid Interface Sci. 2021;596:108–18.
45. Seong C, Mane P, Bae H, Lee S, Kang SH, Ryu SW, Ha JS. Simple fabrication of $BiVO_4$ thin films synthesized by modified SILAR method: effect of film thickness. J Electrochem Soc. 2022;169(1):016501.
46. Li Z, Zhang H, Wang D, Gao C, Sun M, Wu Z, He Q. Reconfigurable assembly of active liquid metal colloidal cluster. Angew Chem Int Ed. 2020;59(45):19884–8.